Diffusion Path and Conduction Mechanism of Oxide Ions in Apatite-Type Lanthanum Silicates

Emilie Béchade,[†] Olivier Masson,*[,†] Tomoyuki Iwata,[‡] Isabelle Julien,[†] Koichiro Fukuda,[‡] Philippe Thomas,[†] and Eric Champion[†]

Laboratoire Science des Procédés Céramiques et de Traitements de Surface (SPCTS), UMR 6638 CNRS, Faculté des Sciences et Techniques, Université de Limoges, 123, Avenue Albert Thomas, 87060 Limoges Cedex, France, and Department of Environmental and Materials Engineering, Nagoya Institute of Technology, Nagoya 466-8555, Japan

Received March 20, 2009. Revised Manuscript Received April 17, 2009

Apatite-type lanthanum silicates of general formula $La_{9.33+2x/3}(SiO_4)_6O_{2+x}$ have appeared recently as a new promising class of oxide ion conductors with potential applications as electrolytes for solid oxide fuel cells (SOFCs). They have been shown to demonstrate relatively high oxide ion conductivity at moderate temperatures as well as at low oxygen partial pressures. In this paper, the diffusion pathways and the conduction mechanism of oxide ions in these phases are reinvestigated. This is done by means of atomic scale computer modeling techniques with both semiempirical and bond valence methods. Our results support that oxide ion conduction along the *c*-axis proceeds by an interstitial mechanism. They also support the presence of interstitial sites located within the conduction channel. However, contrarily to recent research, it is shown that the channel oxide ions are involved in the conduction process by a push−pull type mechanism. This mechanism brings into play a cooperative movement of both two adjacent interstitial oxide ions forming a complex defect and the channel oxide ions. This complex defect is shown to move along the *c*-axis via a nonlinear pathway different from the conduction path proposed in literature to date. The calculated migration energy of this mechanism is found to be equal to 0.32 eV, which compares well with activation energy measured along the *c*-axis for $Nd_{9.33}(SiO_4)_6O_2$ single crystals.

1. Introduction

There is currently much scientific interest in developing materials for environment-friendly electrochemical applications and clean energy conversion systems. Among the various materials, oxide ion conductors seem particularly interesting for fuel cells, catalysts, gas sensors, and batteries[1−3] and have motivated many experimental and theoretical studies over the last years.[4,5] In this context, rare-earth apatite materials have appeared recently as a new class of oxide ion conductors with potential applications as electrolytes for solid oxide fuel cells (SOFC).[6−8] They have been shown to demonstrate relatively high oxide ion conductivity at moderate temperatures as well as at low oxygen partial pressures.[9−13] In particular, apatite lanthanum silicates exhibit the highest conductivities, higher than some of the conventional materials such as doped ZrO_2.[14] These materials, of reference formula (oxygen stoichiometric) $La_{9.33}\square_{0.67}(SiO_4)_6O_2$ ($\square$ = vacancy), are isostructural with the well-known hydroxyapatite phases.[15] Their structure can be described as isolated SiO_4 tetrahedra forming two distinct channels parallel to the *c*-axis (see Figure 1). The smallest of these channels contains La2 lanthanum atoms and vacancies, while the largest ones contain both the La1 lanthanum atoms and the O4 oxide ions. These latter are the only oxide ions that are not a member of the silicon tetrahedra. They are located in the center of equatorial triangles of lanthanum La1 (i.e., on the channel axis). The largest channels are sometimes referred as conduction channels.

Since the first report of Nakayama et al.,[6−8] there have been a number of studies on optimizing both the synthesis

* Corresponding author. E-mail: olivier.masson@unilim.fr.
[†] Université de Limoges.
[‡] Nagoya Institute of Technology.

(1) Lacorre, P.; Goutenoire, F.; Bohnke, O.; Retoux, R.; Laligant, Y. *Nature* **2000**, *404*, 856–858.
(2) Steele, B. C. H.; Heinzel, A. *Nature* **2001**, *414*, 345–352.
(3) Shao, Z.; Haile, S. M. *Nature* **2004**, *431*, 170–173.
(4) Boivin, J. C.; Mairesse, G. *Chem. Mater.* **1998**, *10*, 2870–2888.
(5) Yamamoto, O. *Electrochim. Acta* **2000**, *45*, 2423–2435.
(6) Nakayama, S.; Aono, H.; Sadaoka, Y. *Chem. Lett.* **1995**, *6*, 431–432.
(7) Nakayama, S.; Kageyama, T.; Aono, H.; Sadaoka, Y. *J. Mater. Chem.* **1995**, *5*, 1801–1805.
(8) Nakayama, S.; Sakamoto, M. *J. Eur. Ceram. Soc.* **1998**, *18*, 1413–1418.
(9) Sansom, J. E. H.; Kendrick, E.; Tolchard, J. R.; Islam, M. S.; Slater, P. R. *J. Solid State Electron.* **2006**, *10*, 562–568.
(10) Brisse, A.; Sauvet, A.-L.; Barthet, C.; Georges, S.; Fouletier, J. *Solid State Ionics* **2007**, *178*, 1337–1343.
(11) Arikawa, H.; Nishiguchi, H.; Ishihara, T.; Takita, Y. *Solid State Ionics* **2000**, *136−137*, 31–37.
(12) Shaula, A. L.; Kharton, V. V.; Waerenborgh, J. C.; Rojas, D. P.; Marques, F. M. B. *J. Eur. Ceram. Soc.* **2005**, *25*, 2583–2586.
(13) Shaula, A. L.; Kharton, V. V.; Waerenborgh, J. C.; Rojas, D. P.; Tsipis, E. V.; Vyshatko, N. P.; Patrakeev, M. V.; Marques, F. M. B. *Mater. Res. Bull.* **2004**, *39*, 763–773.
(14) Marques, F. M. B.; Kharton, V. V.; Naumovich, E. N.; Shaula, A. L.; Kovalevsky, A. V.; Yaremchenko, A. A. *Solid State Ionics* **2006**, *177*, 1697–1703.
(15) Kay, M. Y.; Young, R. A. *Nature* **1964**, *204*, 1050–1052.
(16) Higuchi, M.; Kodaira, K.; Nakayama, S. *J. Cryst. Growth* **1999**, *207*, 298–302.
(17) Higuchi, M.; Katase, H.; Kodaira, K.; Nakayama, S. *J. Cryst. Growth* **2000**, *218*, 282–286.
(18) Higuchi, M.; Masubuchi, Y.; Nakayama, S.; Kikkawa, S.; Kodaira, K. *Solid State Ionics* **2004**, *174*, 73–80.

10.1021/cm900783j CCC: $40.75
Published on Web 05/11/2009

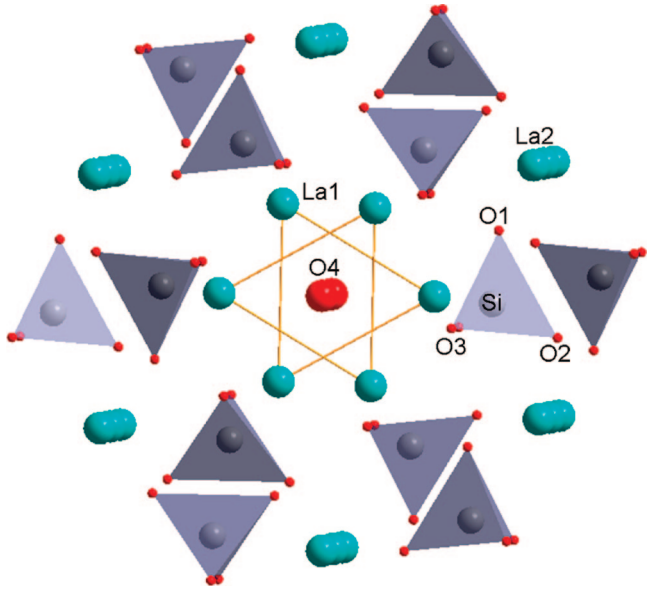

Figure 1. View down the *c*-axis of the $La_{9.33}(SiO_4)_6O_2$ structure showing SiO_4 tetrahedra, La2 channels, and the La1/O4 conduction channel. La2 vacancies are not shown. The two O4 oxide ions of the unit cell are located at the center of the two La1 triangles drawn in this figure.

(of single crystal or polycrystalline samples) and the ionic conductivity of these systems.[16−25] Possibilities of substituting La and Si sites and their effect on conductivities were investigated.[26−36] These materials have been found to be tolerant to a broad range of dopants, with the measured conductivity being very sensitive to the doping regime and cation/anion nonstoichiometry. Among the main results, it was shown that fully stoichiometric systems, such as $La_8Sr_2(SiO_4)_6O_2$, exhibit poor conductivity, whereas conductivities are markedly enhanced in samples containing oxygen excess and/or vacancies at the rare earth site, such as $La_{9.33+2x/3}(SiO_4)_6O_{2+x}$ ($x \geq 0$). These results soon suggested the importance of possible local disorder in the channel oxygen sites. In particular, the displacement of some channel O4 oxygen atoms into interstitial positions was proposed.[37]

Without doubt, further improvement of the performance of these materials needs a better understanding of the ion transport mechanisms. For this, computer modeling at the atomic level is essential as it allows getting insight into the conduction mechanism (where experimental methods often fail). This point has already been tackled but there is still little work regarding the modeling of oxide ion mobility. There is to date only one study dealing with atomistic simulation of the oxide ion transport mechanism along the *c*-axis in the $La_{9.33}(SiO_4)_6O_2$ phase.[38,39] It is based on semiempirical methods and predicts that oxide ion conduction proceeds via an interstitial mechanism with a complex sinusoidal migration pathway at the periphery of the conduction channels. It also predicts the presence at the channel periphery of an energetically favorable oxygen interstitial site. This work has been recently extended by the same research group[40] to the case of the oxygen-excess $La_{9.67}(SiO_4)_6O_{2.5}$ phase. Similar conclusions are drawn, namely, that the interstitial oxide ions move along a complex migration pathway at the periphery of the conduction channel. In addition, it is proposed that the incorporation of interstitial oxide ions induces the formation of distorted SiO_5 units.

Nowadays there is consensus on the existence of interstitial oxide ions in oxygen-excess phases. The case of oxygen-stoichiometric $La_{9.33}(SiO_4)_6O_2$ induced more controversies. Evidences of the presence of interstitial oxide ions were mainly provided by means of neutron powder diffraction (NPD) experiments[41−46] on various oxygen hyperstoichiometric and oxygen-stoichiometric apatites from low (4 K) to higher temperatures (1173 K). Justifications mostly came from the fact that improved fit of experimental data are obtained when taking into account the interstitial site. More indirect evidence like the increase of the O4 anisotropic

(19) Béchade, E.; Julien, I.; Iwata, T.; Masson, O.; Thomas, P.; Champion, E.; Fukuda, K. *J. Eur. Ceram. Soc.* **2008**, *28*, 2717–2724.
(20) Panteix, P. J.; Julien, I.; Bernache-Assollant, D.; Abélard, P. *Mater. Chem. Phys.* **2006**, *95*, 313–320.
(21) Rodriguez-Reyna, E.; Fuentes, A. F.; Maczka, M.; Hanuza, J.; Boulahya, K.; Amadore, U. *J. Solid State Chem.* **2006**, *179*, 522–531.
(22) Tao, S.; Irvine, J. T. S. *Mater. Res. Bull.* **2001**, *36*, 1245–1258.
(23) Masubuchi, Y.; Higuchi, M.; Takeda, T.; Kikkawa, S. *J. Alloys Compd.* **2006**, *408−412*, 641–644.
(24) Celerier, S.; Laberty-Robert, C.; Long, J. W.; Pettigrew, K. A.; Stroud, R. M.; Rolisson, D. R.; Ansart, F.; Stevens, P. *Adv. Mater.* **2006**, *18*, 615–618.
(25) Chesnaud, A.; Bogicevic, C.; Karolak, F.; Estournès, C.; Dezanneau, G. *Chem. Commun.* **2007**, *15*, 1550–1552.
(26) Slater, P. R.; Sansom, J. E. H. *Solid State Phenom.* **2003**, *90−91*, 195–200.
(27) Slater, P. R.; Sansom, J. E. H.; Tolchard, J. R. *Chem. Rec.* **2004**, *4*, 373–384.
(28) Najib, A.; Sansom, J. E. H.; Tolchard, J. R.; Slater, P. R.; Islam, M. S. *Dalton Trans.* **2004**, *19*, 3106–3109.
(29) Abram, E. J. D.; Sinclair, C.; West, A. R. *J. Mater. Chem.* **2001**, *11*, 1978–1979.
(30) Panteix, P. J.; Julien, I.; Abelard, P.; Bernache-Assollant, D. *J. Eur. Ceram. Soc.* **2008**, *28*, 821–828.
(31) Panteix, P. J.; Béchade, E.; Julien, I.; Abélard, P.; Bernache-Assollant, D. *Mater. Res. Bull.* **2008**, *43*, 1223–1231.
(32) Kharton, V. V.; Shaula, A. L.; Patrakeev, M. V.; Waerenborgh, J. C.; Rojas, D. P.; Vyshatko, N. P.; Tsipis, E. V.; Yaremchenko, A. A.; Marques, F. M. B. *J. Electrochem. Soc.* **2004**, *151*, A1236.
(33) Yoshioka, H.; Tanase, S. *Solid State Ionics* **2005**, *176*, 2395.
(34) Chesnaud, A.; Dezanneau, G.; Estournès, C.; Bogicevic, C.; Karolak, F.; Geiger, S.; Geneste, G. *Solid State Ionics* **2008**, *179*, 1929–1939.
(35) León-Reina, L.; Martin-Sedeño, M. C.; Losilla, E. R.; Cabeza, A.; Martinez-Lara, M.; Bruque, S.; Marques, F. M. B.; Sheptyakov, D. V.; Aranda, M. A. G. *Chem. Mater.* **2003**, *15*, 2099–2108.
(36) León-Reina, L.; Losilla, E. R.; Martinez-Lara, M.; Martin-Sedeño, M. C.; Bruque, S.; Núñez, P.; Sheptyakov, D. V.; Aranda, M. A. G. *Chem. Mater.* **2005**, *17*, 596–600.
(37) Sansom, J. E. H.; Riching, D.; Slater, P. R. *Solid State Ionics* **2001**, *139*, 205–210.
(38) Tolchard, J. R.; Islam, M. S.; Slater, P. R. *J. Mater. Chem.* **2003**, *13*, 1956–1961.
(39) Islam, M. S.; Tolchard, J. R.; Slater, P. R. *Chem. Commun.* **2003**, 1486–1487.
(40) Jones, A.; Slater, P. R.; Islam, M. S. *Chem. Mater.* **2008**, *20*, 5055–5060.
(41) León-Reina, L.; Losilla, E. R.; Martinez-Lara, M.; Bruque, S.; Llobet, A.; Sheptyakovc, D. V.; Aranda, M. A. G. *J. Mater. Chem.* **2005**, *15*, 2489–2498.
(42) León-Reina, L.; Porras-Vasquez, J. M.; Losilla, E. R.; Sheptyakov, D. V.; Llobet, A.; Aranda, M. A. G. *Dalton Trans.* **2007**, *205*, 2058–2064.
(43) León-Reina, L.; Losilla, E. R.; Martinez-Lara, M.; Bruque, S.; Aranda, M. A. G. *J. Mater. Chem.* **2004**, *14*, 1142–1149.
(44) León-Reina, L.; Porras-Vázquez, J. M.; Losilla, E. R.; Aranda, M. A. G. *Solid State Ionics* **2006**, *177*, 1307–1315.
(45) Tolchard, J. R.; Slater, P. R. *J. Phys. Chem. Solids* **2008**, *69*, 2433–2439.
(46) Ali, R.; Yashima, M.; Matsushita, Y; Yoshioka, H.; Ohoyama, K; Izumi, F. *Chem. Mater.* **2008**, *20*, 5203–5208.

displacement parameters[42,47] or the change in size of the oxide channel,[48] that is, La1 and O3 triangle sizes, with the amount of oxygen excess were also given. The positions determined experimentally generally accord well with the two atomistic simulation studies. In particular they are found to be situated at the periphery of the oxide channel. These positions seem to be supported by recent ^{29}Si NMR investigations of a range of apatite silicates.[49] Oxygen-excess phases indeed exhibit a clear extra-peak in the ^{29}Si NMR spectra, which is at present attributed to a silicate group adjacent to an interstitial oxygen site (with short Si−O5 bond lengths). However, it is worth noting that this NMR extra-peak is also apparent for the series $La_{8+x}Sr_{2-x}(SiO_4)_6O_{2+x/2}$,[50] for which interstitial positions nearer the channel axis, that is, further away from SiO_4 tetrahedra, were found at room and low temperatures.[42,44] In addition, recent studies based on NPD suggest a more random distribution of interstitial oxygen position.[51,52] Consequently, the exact position of the interstitial site is still not clear. Another point of concern with the results of the two atomistic simulation studies is that, contrarily to what is proposed by some authors,[18,46,51,53−55] O4 ions do not directly participate in the conduction mechanism along the *c*-axis. They can only be seen as a possible "reservoir" for the creation of interstitial oxide ion defects.[56] This can seem quite surprising as O4 atoms are not tightly bonded to lanthanum triangles as suggested by their fairly large anisotropic atomic displacement parameters U_{33}.

The aim of the present work is to reinvestigate the diffusion pathways and the conduction mechanism of oxide ions in apatite-type lanthanum silicates. For that, atomic scale computer modeling and simulation techniques have been employed. One of them is a semiempirical method which needs accurate interatomic potentials. Unfortunately, up to now there is still a lack of known physical properties, notably dynamical properties, for the $La_{9.33}(SiO_4)_6O_2$ and related phases so that interatomic potential parameters are mostly refined against static structure only and then are not fully validated. For this reason, a complementary method has also been used conjointly for this work. This method is based on the bond valence sum calculations and allows obtaining a diffusion path. In this study, the oxygen stoichiometric $La_{9.33}(SiO_4)_6O_2$ phase is probed only. However, it is expected that the conclusions drawn can also apply for the sample containing oxygen excess. This view is supported by both the similarity of the results obtained for $La_{9.33}(SiO_4)_6O_2$ and $La_{9.67}(SiO_4)_6O_{2.5}$[38,40] samples and the gentle monotonic variation of the activation energies with increasing La/O content in $La_{9.33+2x/3}(SiO_4)_6O_{2+x}$.[26,47]

2. Computational Details

All bond valence-sum and defect energy computations were performed using the structure of the oxygen-stoichiometric $La_{9.33}(SiO_4)_6O_2$ phase. This structure is usually described in the $P6_3/m$ space group.[41,42,53,55,57,58] The less symmetrical subgroups $P6_3$[59] and $P\bar{3}$[37] have also been used to account for local disorder in the conduction channel. For the present work, the $P6_3/m$ space group was found to be adequate, and no difference was noticed with calculations performed with the structures described in the less symmetrical space group.

The partial occupancies of the lanthanum sites were treated within the framework of the mean-field theory so that all interactions are scaled by the site occupancies of the atoms. It is well-accepted[53,55,57,58] that La vacancies are at the La2 sites and hence lie relatively far outside the conduction channels. Consequently, it is expected that such mean-field calculations will capture most important effects about the conduction mechanism inside the channel. This may not be the case for the conduction mechanism perpendicularly to the conduction channel, which can be more affected by the "local" occurrence of La vacancy.

2.1. Defect Energy Calculation. Defect energy calculations were performed within the framework of the Born model for ionic solids using the GULP software.[60] Detailed reviews of these atomistic simulation methods can be found elsewhere.[61] The two-body interactions between ions were modeled with a long-range Coulombic potential plus the Buckingham potential representing short-range Pauli repulsion and van der Waals dispersion forces:

$$V_{ij}(r_{ij}) = \frac{q_i q_j}{r_{ij}} + A_{ij}\exp\left(-\frac{r_{ij}}{\rho_{ij}}\right) - \frac{C_{ij}}{r_{ij}^{\,6}} \qquad (1)$$

where r_{ij} is the interatomic distance, q_i and q_j are the charge of the ions taken equal to their formal oxidation state, and A_{ij}, ρ_{ij}, and C_{ij} are empirically derived parameters. As stated elsewhere, employing such formal charges does not mean that it is assumed that the solid is necessarily fully ionic. In practice, these models work well even for compounds in which there is a significant degree of covalency. A three-body interaction O−Si−O term was also added:

$$V_{3\text{-body}} = \frac{1}{2}k(\theta - \theta_0)^2 \qquad (2)$$

where k is the force constant and θ and θ_0 are respectively the actual and equilibrium O−Si−O bond angles. Although not necessary for reproducing silicate phases, this form of harmonic angle-bending potential has often been employed.[38,62−64] It allows accounting for some rigidity of the SiO_4 tetrahedral units and thus

(47) Yoshioka, H. *J. Alloys Compd.* **2006**, *408−412*, 649–652.
(48) Yoshioka, H. *J. Am. Ceram. Soc.* **2007**, *90*, 3099–3105.
(49) Sansom, J. E. H.; Tolchard, J. R.; Islam, M. S.; Apperley, D.; Slater, P. R. *J. Mater. Chem.* **2006**, *16*, 1410–1413.
(50) Orera, A.; Kendrick, E.; Apperley, D. C.; Orerac, V. M.; Slater, P. R. *Dalton Trans.* **2008**, 5296–5301.
(51) Matsushita, Y.; Izumi, F.; Kobayashi, K.; Igawa, N.; Kitazawa, H.; Oyama, Y.; Miyoshi, S.; Yamaguchi, S. *Nucl. Instrum. Methods Phys. Res.* **2009**, *A600*, 319–321.
(52) Beaudet-Savignat, S.; Vincent, A.; Lambert, S.; Gervais, F. *J. Mater. Chem.* **2007**, *17*, 2078–2087.
(53) Okudera, H.; Masubuchi, Y.; Kikkawa, S.; Yoshiasa, A. *Solid State Ionics* **2005**, *176*, 1473–1478.
(54) Masubuchi, Y.; Higuchi, M.; Katase, T.; Takeda, T.; Kikkawa, S.; Kodaira, K.; Nakayama, S. *Solid State Ionics* **2004**, *166*, 213–217.
(55) Masubuchi, Y.; Higuchi, M.; Takeda, T.; Kikkawa, S. *Solid State Ionics* **2006**, *177*, 263–268.
(56) Kendrick, E.; Islam, M. S.; Slater, P. *Chem. Commun.* **2008**, 715–717.
(57) Iwata, T.; Béchade, E.; Fukuda, K.; Masson, O.; Julien, I.; Champion, E.; Thomas, P. *J. Am. Ceram. Soc.* **2008**, *91*, 3714–3720.
(58) Iwata, T.; Fukuda, K.; Béchade, E.; Masson, O.; Julien, I.; Champion, E.; Thomas, P. *Solid State Ionics* **2007**, *178*, 1523–1529.
(59) Lambert, S.; Vincent, A.; Bruneton, E.; Beaudet-Savignat, S.; Guillet, F.; Minot, B.; Bouree, F. *J. Solid State Chem.* **2006**, *179*, 2602–2608.
(60) Gale, J. D. *J. Chem. Soc., Faraday Trans.* **1997**, *93* (4), 629–637.
(61) Catlow, C. R. A. *Computer Modelling in Inorganic Crystallography*; Academic Press: San Diego, 1997.
(62) Meis, C.; Gale, J. D. *Mater. Sci. Eng., B* **1998**, *57*, 52–61.
(63) Meis, C.; Gale, J. D.; Boyer, L.; Carpena, J.; Gosset, D. *J. Phys. Chem. A* **2000**, *104*, 5380–5387.
(64) Chartier, A.; Meis, C.; Gale, J. D. *Phys. Rev. B* **2001**, *64*, 085110.

Table 1. Potentials Parameters for $La_{9.33}(SiO_4)_6O_2$[62,64,a]

Buckingham	A (eV)	ρ (Å)	C (eV Å^6)
$La^{3+}-O^{2-}$	1439.7	0.3661	0.0
$Si^{4+}-O^{2-}$	1078.00	0.3237	0.0
$O^{2-}-O^{2-}$	22764.00	0.149	32.58

[a] Charges are $O_{core} = +0.86$, $O_{shell} = -2.86$ with $k_{O_{core}-O_{shell}} = 98.67$ eV Å^{-2}, $La_{core} = +3.0$, $Si_{core} = +4.0$. The three-body harmonic potentials are $k_{O_{shell}-Si_{corg}-O_{shell}} = 16.675$ eV rad^{-2} with $\theta_0 = 109.5°$. The potential cut-off is 12 Å.

Table 2. Calculated and Experimental[42] Structural Parameters for $La_{9.33}(SiO_4)_6O_2$

(a) Lattice Constants for $La_{9.33}(SiO_4)_6O_2$

a/b, Å	c, Å
experimental	
9.7158	7.1883
calculated	
9.9089	7.1659

(b) Interatomic Distances

bond	exptl, Å	calcd, Å
Si−O1	1.6186	1.5879
Si−O2	1.6286	1.5949
Si−O3	1.6356	1.5893
La1−O1	2.7266	2.8891
La1−O2	2.4952	2.5393
La1−O3	2.4575	2.4682
La1−O4	2.3174	2.3597
La2−O1 (×3)	2.4907	2.4726
La2−O2 (×3)	2.5467	2.6387
La2−O3 (×3)	2.8572	2.9976
O4−O4	3.5941	3.5824

lowers the possibility of occurrence of less common units such as SiO_5, for example.

The polarization of "soft" oxide ions was taken into account using the effective shell model of Dick and Overhauser.[65] Oxide ions then consist of a charged massless shell, on which all short-range potentials act, connected to the ion core via a harmonic spring (i.e., $V_{core\text{-}shell} = 1/2kr^2$ where k is the spring constant), the sum of the shell and core charges being equal to the ion formal charge.

Defect energies were calculated using the Mott−Littleton approximation, in which the crystal lattice that surrounds the defect is partitioned into two regions.[66] In the inner region, all interactions are treated at an atomistic level and the ions are explicitly allowed to relax in response to the defect, while the remainder of the crystal, where the defect forces are relatively weak, is treated by more approximate quasicontinuum methods. In this way, local relaxation is effectively modeled, and the crystal is not considered simply as a rigid lattice through which ion species diffuse. In the present work, an inner region of 12 Å in radius, which contains more than 480 ions, was found to be adequate for the convergence of the computed energies. All lattice relaxations were performed at constant pressure.

The empirical parameters of the interatomic potential were selected from recent studies on silicate materials.[62,64] They are gathered in Table 1. The simulated structural parameters are compared to the experimental ones in Table 2. As it can be seen, the experimental crystal structure is correctly reproduced with relative deviations of the unit cell edges and volume less than 2% and bond lengths less than 6%. The simulated channel size is slightly larger than the experimental one[37,41,42] by 4% with La1 triangle area equal to 7.23 Å^2 instead of 6.95 Å^2. The agreement is thus overall good.

Table 3. Bond Valence Parameters for the X−O Bonds[71]

bonds	La−O	Si−O
R_{ij}	2.064	1.608
b	0.451	0.432

2.2. Bond Valence-Sum Calculation. The 3D modeling of the conduction pathways of the apatite structure was largely carried out using the bond valence-sum (BVS) method. This method has found wide applicability[67] in solid-state chemistry. It has originally been developed to assess equilibrium positions of atoms in crystal structures. It has then proven to be an invaluable tool for predicting inorganic crystalline structures. More recently it has also been used with success for determining conduction pathways[68,69] and ionic conductivity[70] for both crystals and glasses. The bond valence concept is well-known and documented and, hence, only its main features are summarized here. The valence s_{ij} of a bond between two atoms i and j is defined so that the sum of all the valences received by a given atom i with formal oxidation state V_i obeys the bond valence-sum rule:

$$\sum_j s_{ij} = V_i \tag{3}$$

The bond valence s_{ij} is correlated with the bond length d_{ij} by means of the most commonly adopted expression

$$s_{ij} = \exp[(R_{ij} - d_{ij})/b_{ij}] \tag{4}$$

where R_{ij} and b_{ij} are empirical parameters. Atoms i and j are usually referred as "cation" and "anion", although in this context these terms simply refer to the relative electronegativity of the atoms. The bond valence concept does not require an a priori distinction between covalent and ionic types of bonding.

The methods used for predicting or analyzing possible conduction pathways are based on the underlying postulate that the BVS of a mobile ion tends to match the oxidation state not only for equilibrium sites but also for any site that the ion accesses along its pathway. This straightforwardly leads to model ion transport pathways by the set of points in the structure at which the migrating ion has a BVS as near as possible to its oxidation state. The corresponding pathway then represents the "free volume" that oxide ions can access during migration.

In the present case, the knowledge of the cation positions of the apatite structure allowed us to map the bond valence-sum of oxide ions in the structure, in particular inside the conduction channel. The bond valence parameters used for the X−O bonds (X = cations) are those derived by Adams[71] for ionic conduction analysis. They have the advantage over the conventional parameters[72] of accounting for the influence of higher coordination shells and for the anion polarizability via appropriate choice of b_{ij}. They are given in Table 3. The valence V_O of oxide ions was calculated by summing over every X−O bond within a cutoff radius of 5.5 Å. Then, the valence mismatch $\Delta V = |V_O - 2|$ allows obtaining the oxide ion conduction path, given that pathways of lowest activation energy correspond to those for which the maximum valence mismatch is as small as possible. It must be noted that local lattice relaxations around the migrating ion are not taken into account. In addition, the bond valence-sum rule can to some extend be violated. This is

(65) Dick, B. J.; Overhauser, A. W. *Phys. Rev.* **1958**, *112*, 90.
(66) Mott, N. F.; Littleton, M. J. *Trans. Faraday Soc.* **1938**, *34*, 485–499.
(67) Brown, I. D. *The Chemical Bond in Inorganic Chemistry - The Bond Valence Model*; IUCr, Oxford University Press: New York, 2002.
(68) Adams, S.; Swenson, J. *Phys. Rev. B* **2000**, *63*, 054201.
(69) Adams, S. *Solid State Ionics* **2006**, *177*, 1625–1630.
(70) Adams, S.; Swenson, J. *J. Phys. Rev. Lett.* **2000**, *84*, 4144–4147.
(71) http://kristall.uni-mki.gwdg.de/softBV/ (accessed January 2008).
(72) Brese, N. E.; O'Keeffe, M. *Acta Crystallogr., Sect. B* **1991**, *47*, 192–197.

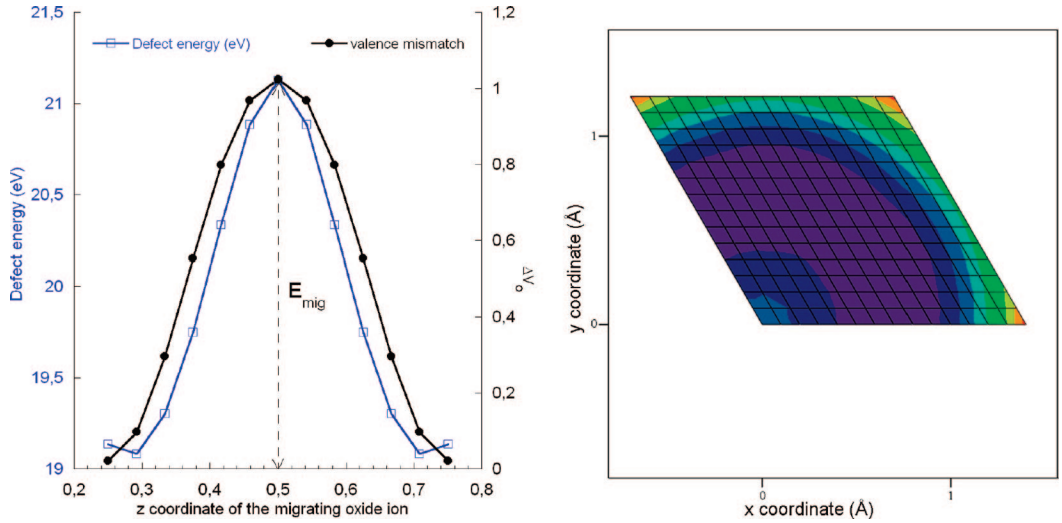

Figure 2. (left) Energy profile of the O4 oxygen vacancy migration along a linear path (blue line) and valence mismatch ΔV_O of a migrating oxide ion along the same linear path (black line). (right) Contour plot of the energy surface in the (a,b) plane at $z = 0.5$ for the O4 oxygen vacancy migration.

the case, for example, for structures with lattice-induced strain.[67] This emphasizes the need that this method be consistent with our defect energy calculations.

Instead of directly plotting the calculated valence mismatch, we chose to graphically represent the diffusion paths by using surface plots of a probability-like density function p_O of presence of oxide ions computed using the following expression:

$$p_O = e^{-(\Delta V/\sigma_1)^2} \tag{5}$$

where σ_1 is an adjustable parameter. Here, the higher the valence mismatch at a particular point, the lower the pseudoprobability of finding a mobile oxide ion at that particular point in space.

As BVS does not consider O−O interactions, the repulsive effect of the tetrahedral oxide ions on the mobile oxide ions was taken into account by using another expression:

$$p_O = e^{-(\Delta V/\sigma_1)^2} \prod_j e^{-((d_{O_j-O_M} - d_{min})/\sigma_2)^2} \tag{6}$$

where σ_2 is also a threshold adjustable parameter. The product is over all the oxide ions O_j of the structure (except O4) for which the distance to the mobile oxide ion O_M is less than a minimum value d_{min}. It allows penalizing the probability of the presence of a mobile oxide ion O_M that is close to tetrahedral oxide ions O_j. The parameters σ_1 and σ_2 are set to minimum values which allow a continuous bond-valence pathway to be defined within the conduction channel or the whole structure. They are to some extent arbitrary but have no major influence on the shape of the pathway. A three-dimensional view of the structure showing the lowest contour surface that provides a continuous path through the structure can be plotted.

Valence map calculations were performed within the unit cell with a mesh of 200^3 grid points using a homemade computer program. The 3D visualizations were done with the Marching cube program.[73,74]

3. Results and Discussion

3.1. Vacancy Migration Mechanism. We start this section with the study of the vacancy migration mechanism. As expected and previously reported,[38] the calculated energy of oxygen vacancy is lower for a vacancy located at the O4 sites ($E_{defect} = 19.05$ eV) than at the O1, O2, or O3 sites (silicate tetrahedra oxide ions) (20.41 eV < E_{defect}< 23.39 eV). Oxygen vacancies are thus more likely to occur at the O4 sites. The energy of the vacancy migration was first estimated by calculating defect energies of oxide ions placed at various positions along a linear path of coordinates (0, 0, z) in the conduction channel between two adjacent vacant O4 sites (of coordinates (0, 0, 1/4) and (0, 0, 3/4)). For each calculation, the migrating oxide ion was held fixed whereas the surrounding structure was allowed to relax to zero force. The energy profile of vacancy migration so obtained is plotted in Figure 2. The energy maximum is found midway between two neighboring O4 sites. The corresponding energy barrier is $E = 2.0$ eV. This high value is about twice the value obtained by Tolchard et al.[38] ($E = 1.1$ eV) for the same path, which emphasizes the large effect of the interatomic potential used. The evolution of the valence mismatch of oxide ions along this linear path was also calculated. Its profile is plotted in Figure 2. It is interesting to note the close resemblance of the two profiles indicating the consistency of the two methods. In particular, the high valence mismatch $|\Delta V_O| > 1$ obtained midway between the two neighboring O4 sites compares well with the high calculated migration energy.

The exact determination of the energy barrier of the vacancy jump requires the value of the defect energy at the saddle point. This point was localized by mapping the migrating oxide ion energy in the (a,b) plane at $z = 0.5$. The corresponding contour plot is shown in Figure 2. As it can be seen, the saddle point is located away from the channel axis, at about 0.5 Å. The corresponding migration energy value is $E_{mig} = 1.85$ eV. It is still high and does not compare with any of the experimental activation energies reported in the literature as well for the polycrystalline samples ($E_a = 0.6-0.8$ eV)[26−36] as for the single-crystal ($E_a = 0.32$ eV for $Nd_{9.33}(SiO_4)_6O_2$ measured

(73) Rohlicek, J.; Husak, M. *J. Appl. Crystallogr.* **2007**, *40*, 600–601.
(74) Husak, M.; Rohlicek, J. http://www.vscht.cz/min/mce/index.html (accessed June 2008).

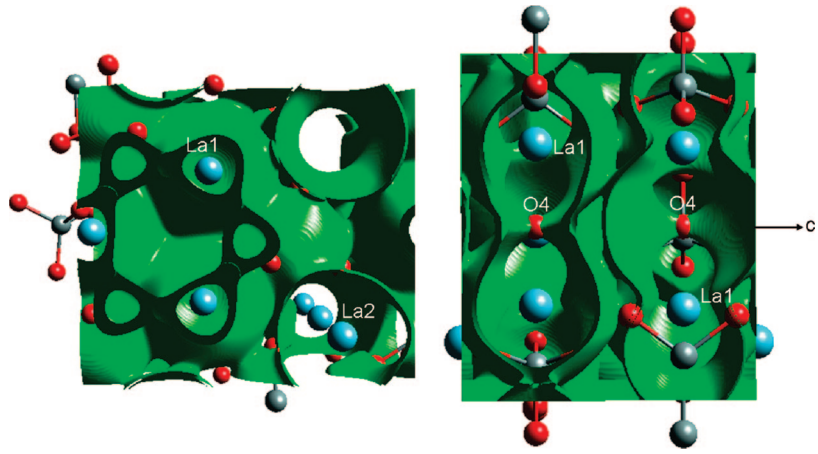

Figure 3. Surface-plot (in green) of the probability-like density function p_O calculated using eq 5: (left) view down to the *c*-axis, (right) view along the *c*-axis.

parallel to the *c*-axis).[75] These results confirm that vacancy migration mechanism is unlikely to occur in this apatite phase.

3.2. Oxide Ion Conduction Pathways. The surface plot of the probability-like density function p_O calculated around the conduction channel using eq 5 is represented in Figure 3 for $p_O = 0.92$. Continuous migration pathways could be obtained for σ_1 set to 0.4. Interestingly, they are continuous along all three directions of space. No σ_1 value allowed obtaining a continuous path in one direction only, notably along the *c*-axis. This result may be correlated with the fact that most experimental ionic conduction activation energies measured parallel and perpendicular to the *c*-axis are similar.[17,75,76] Furthermore, it is clear that the pathway in the conduction channel is not linear and goes through the O4 sites. It starts from an O4 site, moves away from the channel axis, goes through six narrow passages (in the plane $z = 0.5$, i.e. located in the bisector plane of the two adjacent O4 sites), and finally gets the next O4 site. The probability around the *c*-axis in between two adjacent O4 sites is zero. More importantly, it is also zero in the (*a*,*b*) plane around the O4 positions (i.e., at $z = 0.25$ and 0.75). These results suggest that, as proposed by some authors,[18,46,51,53−55] the oxides ions located in the conduction channel at the O4 sites are involved in the conduction mechanism. In addition, this conduction pathway completely differs from that proposed by Tolchard et al.[38] In particular, their "sinusoidal-like" pathway (cf. Figure 4) goes clearly through positions in the (*a*,*b*) planes around the O4 positions where the probability is found to be zero in the present study.

The surface plot of the probability-like density function calculated using eq 6, that is, taking into account the repulsive effect of silicate tetrahedron oxide ions on the migrating ions, is represented in Figure 5. This time, a continuous pathway within the channel only (along the *c*-axis) could be obtained with σ_2 set to 0.63 Å. This path has basically the same features as the previous one. In particular, it is not linear

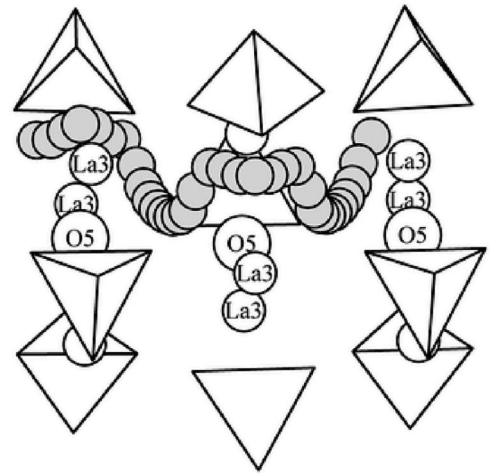

Figure 4. Interstitial oxygen migration along the *c* axis proposed by Tolchard et al.[38] (the O5 sites of this figure correspond to O4 sites in the present study).

and goes through O4 sites and six narrow passages. It is made of two groups of three symmetrical branches. Each group is centered on an O4 site and turned by 60° about the *c*-axis with respect to the following one. Two neighboring groups are connected by the 6 narrow passages at about 1 Å away from the center of the channel.

To compare these results with atomistic calculations, we mapped the defect energy of an extra oxide ion inserted in the channel conduction. Here also, for each calculation the extra oxide ion was held fixed whereas the surrounding structure was allowed to relax to zero force. The three contour plots corresponding to the mapping of the planes $z = 0.42$, 0.5, and 0.58 are shown in Figure 6. The regions of lowest energy are in the dark (purple and blue) colors. For each map, a white cross is placed at the minimum of energy.

Six equivalent minima of energy $E = -11.105$ eV are found 60° degrees apart (from each other) in the plane $z = 0.5$. They lie in a hexagonal ring-shaped basin, at less than 1 Å from the center of the channel. Deeper minima ($E = -11.396$ eV) are found for the maps $z = 0.42$ and $z = 0.58$. For each of these two maps, there are six equivalent minima lying in three double-wells. These wells are symmetrical by 120° about the *c*-axis. Interestingly, the lowest defect energy position is not located in the central plane ($z = 0.5$) but rather

(75) Nakayama, S.; Sakamoto, M.; Higuchi, M.; Kodaira, K. *J. Mater. Sci. Lett.* **2000**, *19*, 91–93.
(76) Nakayama, S.; Sakamoto, M.; Higuchi, M.; Kodaira, K.; Sato, M.; Kakita, S.; Suzuki, T.; Itoh, K. *J. Eur. Ceram. Soc.* **1998**, *19*, 507–510.

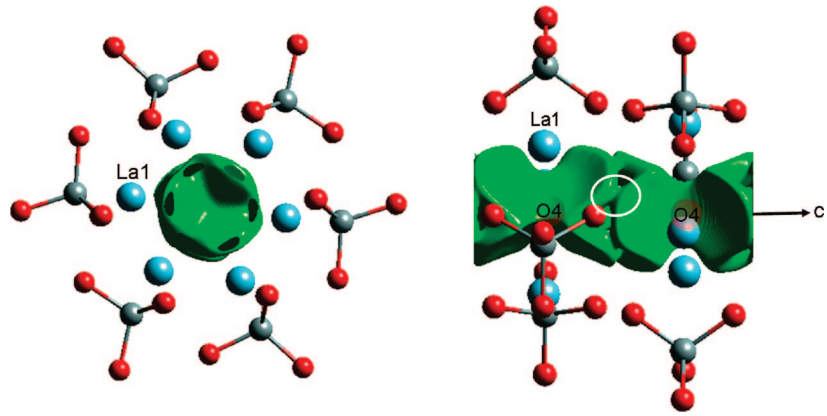

Figure 5. Surface plot (in green) of the probability-like density function p_O calculated using eq 6: (left) view down to the *c*-axis, (right) view along the *c*-axis.

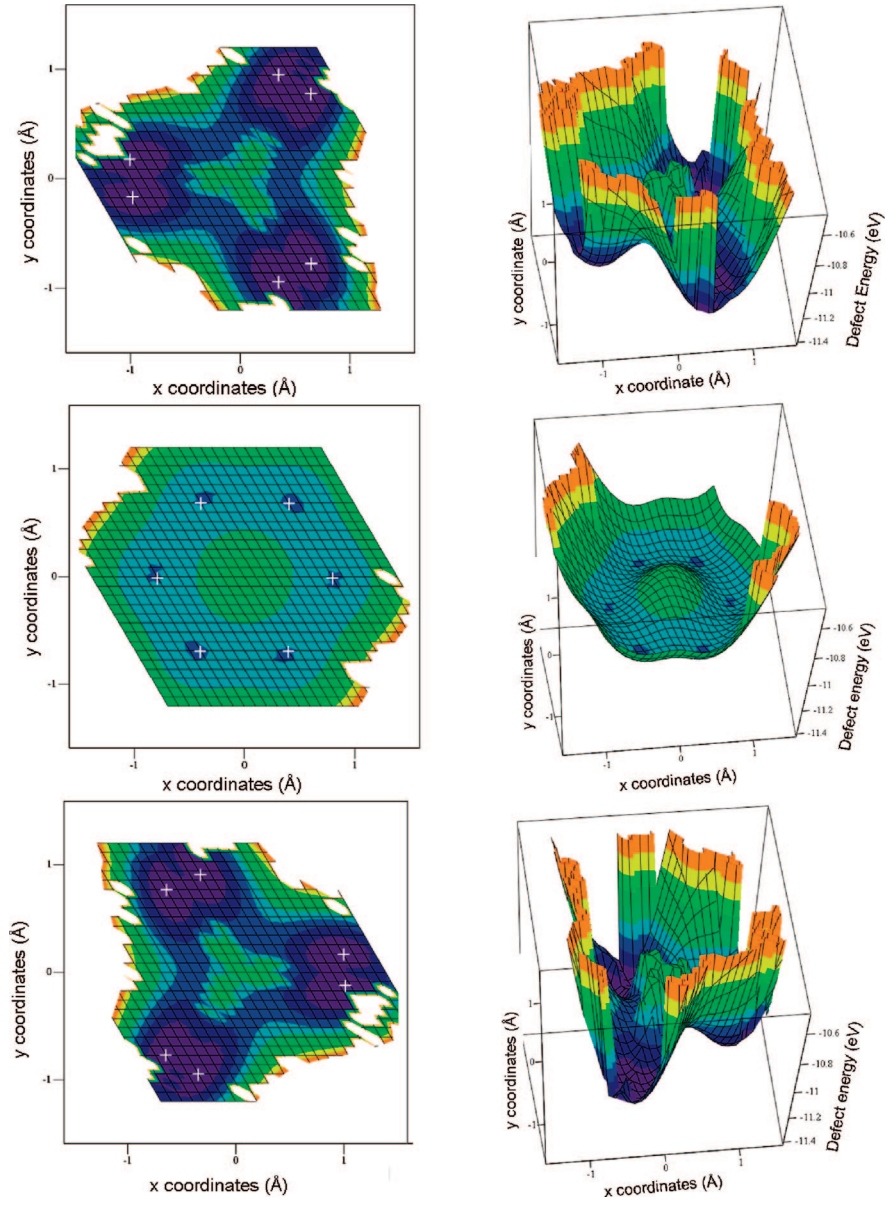

Figure 6. Defect energy maps for an extra oxide ion located in the (*a*,*b*) planes at (from top to bottom) $z = 0.42$, 0.5, and 0.58. (left) Projection along the *z*-axis, (right) perspective view. White crosses locate the minima of energy.

around the planes $z = 0.42$ and 0.58. Moreover, all the energy minima positions and the shape of the basins compare well with the conduction path obtained by the BVS method. The six minima found in the $z = 0.5$ plane for example correspond clearly to the six narrow passages of the conduction pathway. The positions found by the two methods

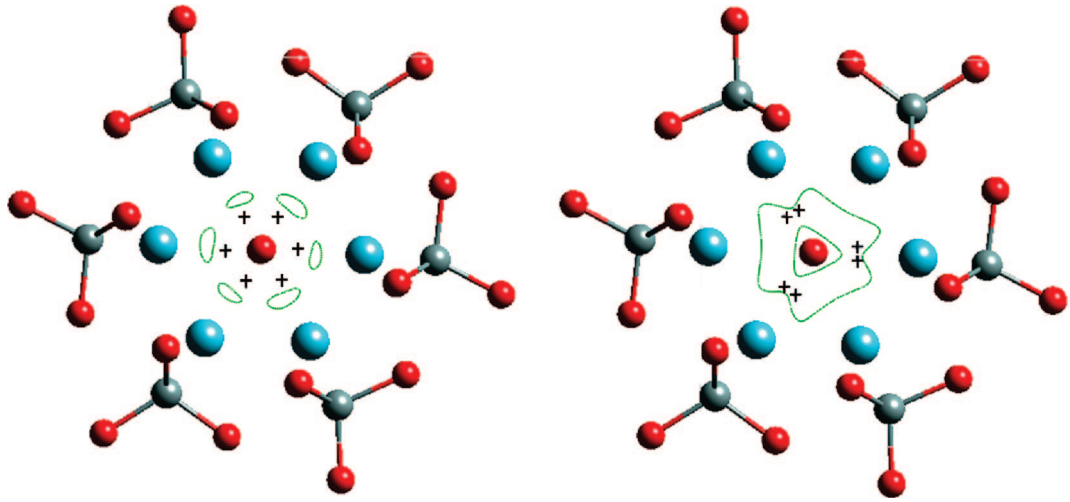

Figure 7. BV pathway contour plot (green lines) in the (a,b) planes at $z = 0.5$ (left) and at $z = 0.58$ (right). Black crosses locate the minima of energy of the defect energy maps.

are close together as one can see in Figure 7. These minima are not deep and thus are consistent with the narrowness of the passages of the pathway in the plane $z = 0.5$. As we will see in the next section, they correspond to the saddle point of the interstitial mechanism. The same resemblance is apparent for the $z = 0.42$ and 0.58 planes. In particular, the three pairs of deeper minima found in each plane are clearly located within the three branches of the conduction pathway. A comparison is also given in Figure 7 for the plane $z = 0.58$. These results emphasize the consistency of the two methods already mentioned previously. In addition, they suggest that the set of interatomic potentials used in this study is certainly able to capture the most important aspects of the conduction mechanism inside the channel.

3.3. Interstitial Sites and Complex Defect ($2O_i''$,$1V_O^{\bullet\bullet}$). In the following, we consider possible regions of lowest energy, namely, interstitial sites. Previous energy maps have already shown that low energy minima are found in the planes $z = 0.42$ and 0.58. We have thus performed defect energy calculations in the vicinity of those minima, but this time the inserted extra oxide ion is allowed to relax. A stable position of energy $E = -11.426$ eV was obtained at coordinate (0.106, 0.0177, 0.588). This site, noted O5, is located within the conduction channel at about 0.96 Å from the channel axis in the plane $z = 0.588$. As one can see in Figure 8, it touches the conduction pathway determined by the BVS method. Note that there are all in all 12 equivalent sites per unit cell within the channel, 3 sites for each of the planes $z = 0.088$, $z = 0.412$, $z = 0.588$, and $z = 0.912$. This site and those determined by neutron diffraction experiments[41−44] on apatite phases of various compositions lie approximately in the same plane, i.e., $z \sim 0.58$. They also lie in the same direction from the channel axis. The O5 site is not located at the very periphery of the channel. It is about 2 times nearer the channel axis than the interstitial position (0, 0.25, 0.58) proposed for the $La_{9.33}(SiO_4)_6O_2$ phase.[41] Consequently, it is too far away from the neighboring SiO_4 groups (at approximately 3 Å from the silicon atoms) for pseudo "SiO_5" units to form as proposed by Jones et al.[40] for the $La_{9.67}(SiO_4)_6O_{2.5}$ composition. It is however close to the

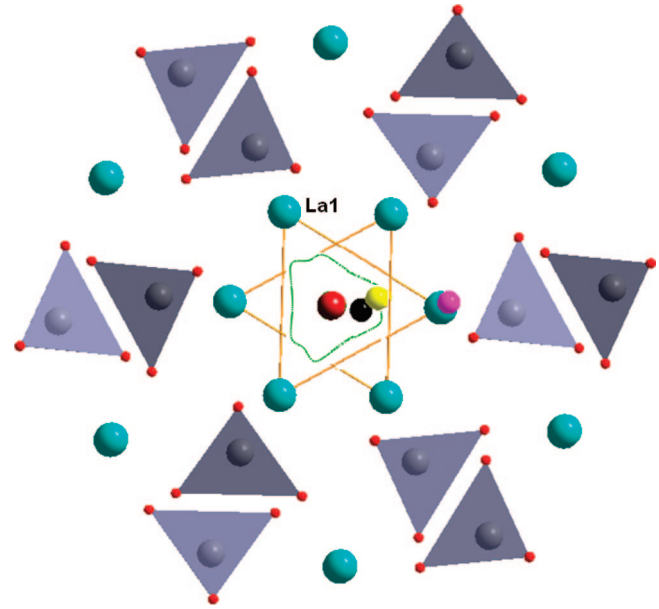

Figure 8. Interstitial position obtained in this study (yellow ball) and determined experimentally by Leon-Reina et al.[41,44] for $La_{8.65}Sr_{1.35}(SiO_4)_6O_{2.32}$ (black ball) and $La_{9.33}(SiO_4)_6O_2$ (pink ball). The BV pathway contour plot in the (*a*,*b*) plane at $z = 0.588$ is drawn in green.

interstitial position (0.014, 0.071, 0.5555) proposed for $La_{8.65}Sr_{1.35}(SiO_4)_6O_{2.32}$ at room (and low) temperature.[44]

Examination of the local structure around the extra oxide ion (Figure 9) reveals many types of structural relaxation. First of all, we can observe rotations and slight distorsions of the nearby SiO_4 tetrahedra. The largest displacement for the O3/O2 oxygen is about 0.53 Å, which is smaller than that reported by Tolchard et al.[38] (1.3 Å for an O3 oxygen). We can also note a decrease of the size of the La1 triangles (from 7.23 Å^2 down to 6.90 Å^2) and an increase of size of the O3 triangles (from 12.28 Å^2 up to 13.50 Å^2). These triangle size variations are in good agreement with the X-ray diffraction measurements by Yoshioka[48] on a series of lanthanum silicate phases. More importantly, we can observe that the insertion of the extra oxide ion at the O5 position results in the displacement of the neighboring O4 oxide ion, which moves to another interstitial position, noted O5′ in

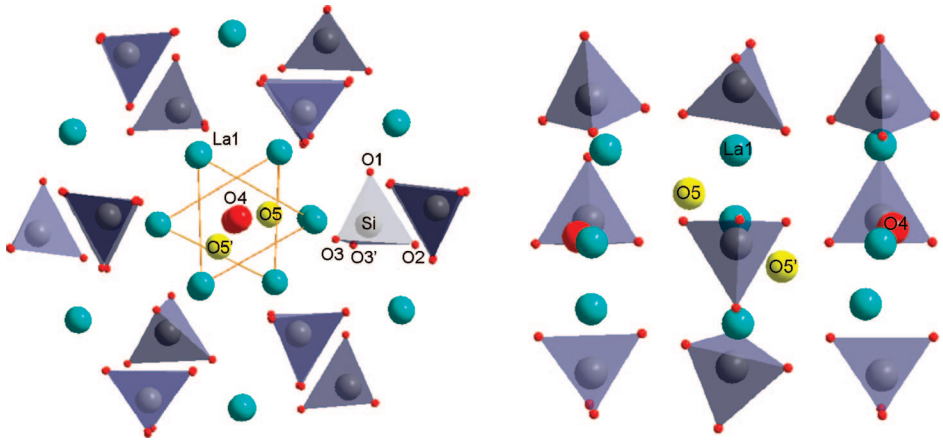

Figure 9. Views of the O5 and O5′ interstitial oxide ions forming the complex defect and the surrounding relaxed structure: (left) view down the *c* axis, (right) view along the *c* axis. Displacements of the adjacent tetrahedral atoms: O1 (0.05 Å), O2 (0.41 Å), O3 (0.05 Å), O3′ (0.53 Å), Si (0.16 Å).

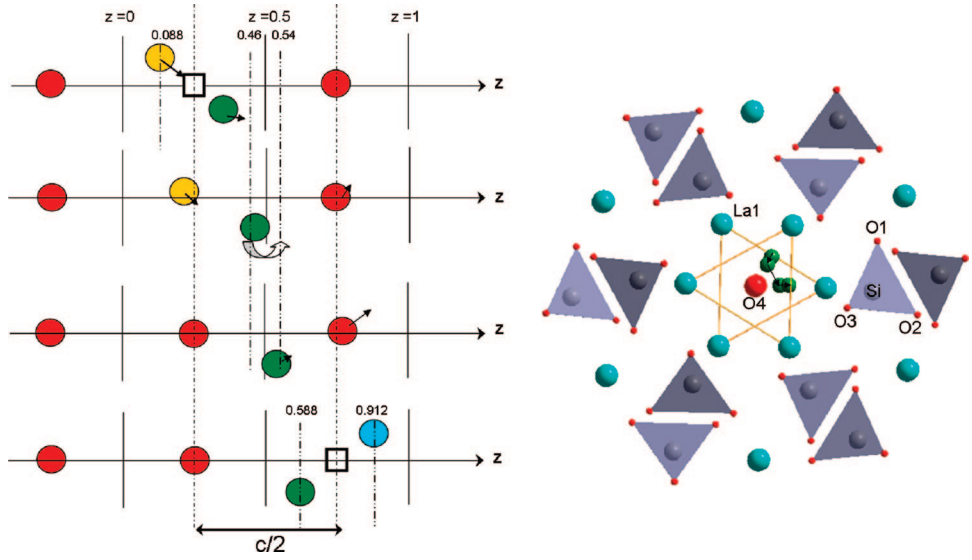

Figure 10. (left) Schematic view of the migration of the ($2O_i''$,$1V_O^{\bullet\bullet}$) complex defect: O4 anions and vacancy are represented by red balls and squares respectively, and O5, O5′, and O5" anions are represented by yellow, green and blue balls respectively. (right) Migration path of the O5′ ion between the positions of coordinates (0.11, 0.11, 0.46) and (0.11, 0, 0.54) (green balls).

Figure 9, of coordinate (−0.0883, −0.106, 0.912) and created an oxygen vacancy. This leads to the formation of a complex defect made of two interstitial oxide ions 2.93 Å apart and separated by an anion vacancy, noted ($2O_i''$,$1V_O^{\bullet\bullet}$) in the Kroger-Vink notation. It is worth noting that the presence of this defect in the apatite structure is consistent with most of the observations made by diffraction experiments like the change of La1 or O3 triangle sizes, interstitial positions (as stated above), and also the large anisotropic (along the *c* axis) displacement parameters U_{33}. This latter point is particularly important as it supports that the large value of U_{33}, especially at room and lower temperatures, can partly result from local atomic displacements caused by the presence of interstitial oxide ions. Another feature that is a consequence of the presence of the complex defect is that for each extra oxide ion inserted in the structure, there are actually two interstitial ions formed.

3.4. Mechanism and Energy of Migration of the Complex Defect. We now consider the migration mechanism, and the associated energy, of this complex defect. This mechanism was determined by performing the following defect calculations. First, an extra oxide ion was inserted at coordinates (0.0, −0.011, 0.04) which led, after relaxation of the local structure, to the formation of a complex defect with two anions O5 and O5′ at coordinates (0.018, −0.088, 0.088) and (0.088, 0.106, 0.412). The O5′ anion was then displaced toward the neighboring interstitial position. For each step of displacement, the O5′ ion was held fixed whereas the surrounding structure was allowed to relax to zero force. In addition, for each *z* coordinate, several positions in the (*a*,*b*) plane were tested to find the lowest-energy position. The different steps of migration of the complex defect, so obtained along half the *c* cell-edge, are schematically illustrated in Figure 10. The maximum of energy is reached when O5′ goes through the saddle point of coordinate (0.08, 0, 0.5) corresponding approximately to one of the six narrow passages located in the plane $z = 0.5$. During this displacement, the O5′ ion turns by 60° about the channel axis (Figure 10), and at the same time, the O5 interstitial anion returns to the vacant normal O4 site at coordinate (0, 0, 1/4). To finish, the O5′ ion gets the neighboring O5′ site of coordinate (0.106, 0.0177, 0.588) and the ion located at the O4 site of coordinate (0, 0, 3/4) moves to the neighboring interstitial O5″ site at (−0.0883, −0.106, 0.912). The complex defect

is thus formed again but is half the *c* cell edge further away from the starting position. As it can be seen, this displacement involves a cooperative movement of both the complex defect and the channel oxide ions and brings into play a push−pull type mechanism. The associated migration energy E_{mig} is about 0.32 eV. This value is much lower than that calculated for the vacancy migration mechanism. It is also in good agreement with most of experimental activation energies reported in literature. In particular it is very close to the value (0.31 eV) measured along the *c*-axis by Nakayama et al.[75] for a $Nd_{9.33}(SiO_4)_6O_2$ single crystal. It is worth noting that although no experimental activation energies are reported for the $La_{9.33}(SiO_4)_6O_2$ single crystal, the values of both conductivities and activation energies of $Nd_{9.33}(SiO_4)_6O_2$ and $La_{9.33}(SiO_4)_6O_2$ polycrystalline samples are nearly identical.

3.5. Formation Energy of the Complex Defect. To finish, we consider the energy of formation of the complex defect. This is an important point as experimental activation energy values deduced from the Arrhenius plot generally cannot readily be compared with migration energy. Indeed, the former generally also contains a part of the energy of defect formation. This should be the case for the oxygen stoichiometric $La_{9.33}(SiO_4)_6O_2$ phase as it is expected that the formation of the complex defect be thermally activated. On the contrary, it should not be for oxygen-excess $La_{9.33+2x/3}(SiO_4)_6O_{2+x}$ ($x > 0$) phases, as defects are expected to be natively present with content varying according to x.

The energy of formation of the complex defect was computed according a simple Frenkel-type defect formation. In Kroger-Vink notation, this takes the form:

$$2O_O^x \rightarrow V_O^{\bullet\bullet} + (2O_i'', V_O^{\bullet\bullet})$$

The combination of individual defect energies, that is, vacancy and complex defect, allowed obtaining the following value of the complex defect formation energy: $E_f = 3.8$ eV/defect^{-1}. This value is high in comparison to the experimental activation energy values measured on both single- and polycrystals. This suggests that the complex defect is unlikely to arise from this Frenkel-type disorder and other mechanisms of formation have to be found. For example, it has been recently suggested[52] on the basis of TEM study that sintered $La_{9.33}(SiO_4)_6O_2$ material may contain local composition variation with oxygen deficient $La_{9.33-\varepsilon}(SiO_4)_6O_{2-\delta}$ and oxygen excess $La_{9.33+\varepsilon}(SiO_4)_6O_{2+\delta}$ domains. This could explain the presence of such a defect in the oxygen excess domains.

4. Conclusions

Atomic scale computer modeling techniques comprising both semiempirical and bond valence methods have been conjointly used to investigate the oxide ion transport mechanism and pathways in apatite-type lanthanum silicates. The main points are summarized as follows:

(1) Oxide ion migration occurs via an indirect-interstitial mechanism.

(2) There exists an interstitial site located within the conduction channel. This site of coordinates (0.106, 0.0177, 0.588) does not lie at the very periphery of the channel but is more inside the channel than most of positions determined experimentally by diffraction techniques. It is however close to the interstitial position (0.014, 0.071, 0.5555) proposed for $La_{8.65}Sr_{1.35}(SiO_4)_6O_{2.32}$.

(3) Interstitial oxide ion induces rotation of nearby SiO_4 tetrahedra, a decrease of the La1 triangle sizes, and an increase of size of the O3 triangles. Most importantly, it induces the displacement of the neighboring O4 oxide ion to a next interstitial position, so forming a complex defect ($2O_i''$,$1V_O^{\bullet\bullet}$).

(4) The channel oxide ions are involved in the conduction process by a push−pull type mechanism. This mechanism brings into play a cooperative movement of both the complex defect and the channel oxide ions. The calculated migration energy of this mechanism is found to be equal to 0.32 eV, which compares well with activation energy measured along the *c*-axis for $Nd_{9.33}(SiO_4)_6O_2$ single crystals.

(5) Oxide ions migration along the *c*-axis follows a nonlinear pathway which contains both the O4 sites and the interstitial sites. It is different from the "sinusoidal-like" conduction path proposed in literature to date.

Acknowledgment. E.B. is grateful to the Conseil Régional du Limousin for financial support.

Note Added after ASAP Publication. Due to a production oversight, this paper published ASAP May 11, 2009 with errors in Tables 1 and 2; the corrected paper published ASAP May 14, 2009.

CM900783J